Natural Hazards
https://doi.org/10.1007/s11069-023-06013-x

ORIGINAL PAPER

# High-resolution seismic characterization of post-glacial subaqueous mass movements in the Beagle Channel (Tierra del Fuego, Argentina): dynamics and tsunami hazard implications

**Donaldo Mauricio Bran[1,2] · Fermín Palma[1,2] · Sebastián Principi[1,2] · Emanuele Lodolo[3] · Luca Baradello[3] · Jorge Gabriel Lozano[1,2] · Alejandro Alberto Tassone[1,2]**

Received: 6 September 2022 / Accepted: 27 April 2023


## Abstract

Analysis of high-resolution seismic profiles from the central Beagle Channel enabled the recognition and characterization of several post-glacial subaqueous mass transport deposits in the subsurface of Bahía Ushuaia, offshore the city of Ushuaia (Argentina). These deposits are located at different stratigraphic levels and are embedded in the stratified sedimentary sequence within a deep trough, suggesting a recurrent occurrence. Up to eleven deposits have been identified, with four major events that involved estimated sediment volumes ranging from 12 to 57 million $m^3$. The latter are associated with megaturbidite deposits up to 10 m thick. Two of the largest events postdate the early Holocene unconformity of marine transgression. The seismic data suggest a different dynamic behaviour of these four main events, with erosional, strongly disintegrating and longer-lasting pre-marine transgression mass transport events compared to the post-early Holocene deposits. Several of the deposits appear to have a common origin due to earthquake-induced failures of submerged glaciofluvial deposits or from tributary deltas. In addition, a preliminary analysis of the potential generation of tsunami waves associated with the largest submarine failures was carried out using numerical models. The results show that at least three of them would have the potential to generate dangerous waves with maximum heights of up to 1–2 m in the port of Ushuaia and estimated run-up heights between 2 and 8 m. Although further detailed analysis is recommended, particularly with regard to a more sophisticated modelling approach and refinement of the resolution of bathymetric and topographic data for strategic areas.

✉ Donaldo Mauricio Bran
dbran@gl.fcen.uba.ar

[1] Departmento de Ciencias Geológicas, Facultad de Ciencias Exactas y Naturales, Universidad de Buenos Aires, Buenos Aires, Argentina

[2] CONICET-Universidad de Buenos Aires, Instituto de Geociencias Básicas, Aplicadas y Ambientales de Buenos Aires (IGeBA), Buenos Aires, Argentina

[3] Istituto Nazionale di Oceanografia e di Geofisica Sperimentale (OGS), Trieste, Italy

Published online: 18 May 2023

**Keywords** Mass transport deposits · Seismics · Megaturbidite · Tsunami

## 1 Introduction

Fjords usually have well-preserved sedimentary sequences, which are important records for the study of land–sea interactions during Quaternary glaciation and environmental changes that occurred during deglaciation (Syvitski et al. 1987). These flooded, formerly glaciated valleys are also known for their high sedimentation, rugged relief and steep delta fronts, making them susceptible to generate mass transport deposits (MTDs) (Syvitski et al. 1987; Hampton et al. 1996; Masson et al. 2006; Bellwald et al. 2019). Indeed, these deposits could account for up to two-thirds of the fjord basin fill (Bellwald et al. 2016). The importance of studying MTDs lies in their role as transfers of sediments from the land to the ocean, their importance as proxies for climate and sea-level changes and for the development of palaeoseismic records (Tappin 2010; St-Onge et al. 2012; De Batist et al. 2017). In addition, subaqueous mass movements can trigger tsunami waves (Masson et al. 2006; Harbitz et al. 2014), which pose a major threat to coastal settlements.

The southern part of Tierra del Fuego is characterized by an archipelago landscape in which islands are separated by fjords and channels. In general, studies conducted along the flooded valleys of the area have focused on their syn- and post-glacial sedimentary evolution and deglacial history (Bujalesky et al. 2004; Boyd et al. 2008; Fernández et al. 2017). In the Beagle Channel, previous studies have indicated the importance of MTDs for deep-water sedimentation (Isla et al. 1999; Bujalesky et al. 2004), although no characterization of this type of sediment has been carried out in the area to date.

We conducted a high-resolution seismic reflection survey in Bahía Ushuaia, a north-west-facing bay in the Beagle Channel, to analyse post-glacial depositional processes and characterize a series of subaqueous mass transport events preserved in the sedimentary sequence of the bay. The data presented here allowed an assessment of their likely sources, trigger mechanisms and depositional processes. In addition, a preliminary assessment of their tsunami potential was made through numerical modelling. This study represents a first approach to the analysis of the geohazards posed by subaqueous mass movements in the area and underlines the need for future research.

### 1.1 Geo-stratigraphic framework

The Beagle Channel (BC) is a bi-national waterway connecting the Atlantic and Pacific Oceans, located south of Isla Grande de Tierra del Fuego (IGTdF) (Fig. 1A). The BC is a flooded tectonic valley with estuarine dynamics, with semi-diurnal tides averaging 1.1 m in the Ushuaia area (Isla et al. 1999). It has a short fetch to the main south-westerly winds with occasional gusts generating small surf waves up to 0.5 m high (Bujalesky 2007).

The BC extends along a major sinistral fault related to the Scotia–South American plate boundary, represented in Tierra del Fuego by the Magallanes–Fagnano fault system to the north (Lodolo et al. 2003; Menichetti et al. 2008). During the Quaternary, the channel was extensively and successively glaciated (Rabassa et al. 2000, 2011) with a maximum extent of ice lobes during the Last Glacial Maximum at 25 to 18 kyr BP (Rabassa et al. 2000). Glacial retreat began at about 18 kyr BP (Heusser 1993; Hall et al. 2013), while proglacial lakes and glaciofluvial systems developed along the ice-free trough (Bujalesky et al. 2004).

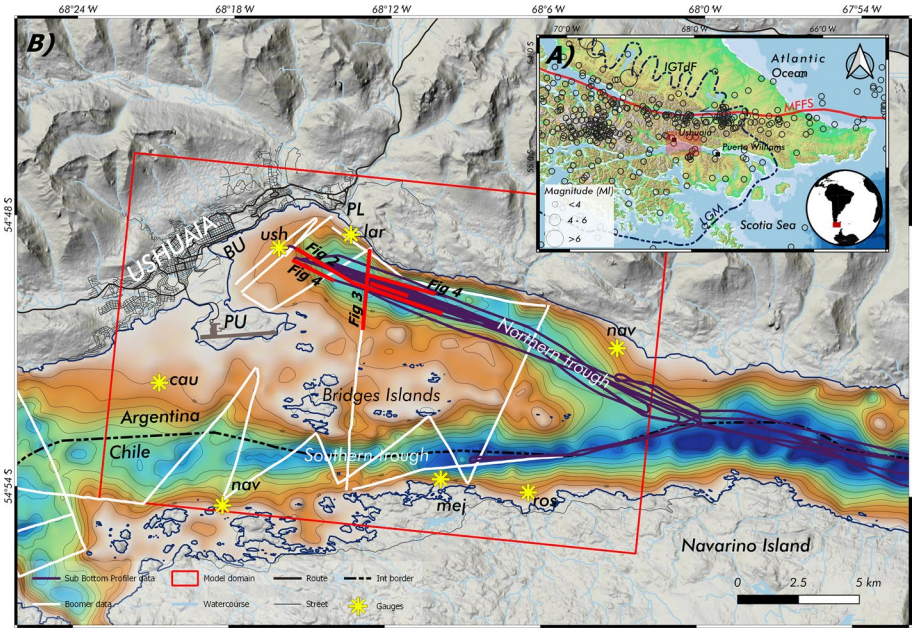


**Fig. 1** **A** Map showing the location of the study area on Isla Grande de Tierra del Fuego. The dashed line represents the maximum extent of glaciers during the Last Glaciation (Hall et al. 2013). The empty circles represent the epicentres of earthquakes taken from the Tierra del Fuego Reference Standard Earthquake Catalogue (Sabbione et al. 2007; Connon et al. 2021). The transform plate boundary, the Magallanes-Fagnano fault system (MFFS), is shown in red. **B** Central Beagle Channel showing the location of the seismic dataset used in this work: boomer (white line), sub-bottom profiler (purple line). The line segments presented in this article are depicted as red lines. The red rectangle represents the modelling domain. A set of synthetic gauges is shown as yellow stars. The bathymetric digital elevation model is from Esteban et al. (2013). *BU* Bahia Ushuaia; *PL* Playa Larga; *PU* Peninsula Ushuaia

The marine transgression event and the establishment of the present channel environment would have occurred during the early Holocene (Rabassa et al. 1986; Candel et al. 2018).

The central segment of the BC undergoes a N-S widening and forms a broad, semicircular NW–SE-oriented embayment, known as Bahía Ushuaia (BU) (Fig. 1B). At the tip of the bay is the city of Ushuaia, a densely populated area with several buildings and infrastructure for maritime and air transport along the coast. Smaller settlements are located south of BU, along the Chilean coast, such as Puerto Navarino and Puerto Williams (east of the study area). The BU has a rugged submarine topography with a deep longitudinal NW–SE at the northern edge of the bay (northern trough, Fig. 1), separated from the deep southern main channel axis by a shallow sill (< 40 m) (Esteban et al. 2013). The sill is the offshore continuation of the Ushuaia Peninsula and constituted by a bedrock high that partially emerges as a small archipelago of islands in the central part of the channel (Fig. 1B).

The BC seismic stratigraphy was adapted from the stratigraphy proposed by Bujalesky et al. (2004) and Bran (2020), in which six seismic units are recognized, although only four of them are present on the seismic lines in the study area. The layered basin fill, with horizontal to slightly SE dipping reflections, onlap against an acoustically transparent bedrock, formed by the Mesozoic metasedimentary rocks of Yaghan and Lemaire Formations, or towards a chaotic to hummocky glacial deposits (Unit 1). The basal layered succession

(Unit 2) is constituted by medium-to-low amplitude laterally onlapping reflections, interpreted as ice-contact glaciolacustrine deposits, which filled the irregular deglacial topography. The oldest ages for the glaciolacustrine deposits are *ca.* 16 cal kyrs BP, obtained from lagoonal cores in the northern shore of Navarino Island (McCulloch et al. 2020). The Unit 3 is constituted by high-amplitude reflections interbedded with semi-transparent layers and represents a sequence of gravity flows and turbidites resulting from glaciofluvial-derived bottom currents flowing into an ice-distal glaciolacustrine environment from the main inlet deltas located at the bay's head. The transition to the uppermost Unit 4 is interpreted as the change from glaciolacustrine to the present-day marine conditions, dated from onshore cores and deposits as *ca*. 8.5 cal kyrs BP (Rabassa et al. 1986; Candel et al. 2018; McCulloch et al. 2019). The medium-to-high-amplitude parallel reflections with a drape geometry depicts fine sediments derived from buoyant over/interflow plumes into a saline environment. The acoustic fabric becomes semi-transparent towards the head of the bay, depicting not only the shallowing of the basement but also the presence of a tabular-shaped transparent to roughly stratified package that corresponds to a submerged glaciofluvial plain, observed as a shallow flat area (< 30 m b.s.l) in the bathymetry (Fig. 1). In front of the glaciofluvial plain, a slope break with an average inclination of 7° dips towards the deep (~ 140 m b.s.l.) basin floor.

## 2 Methods

### 2.1 Seismic survey

The sub-bottom profiler data were collected on board the *RV Austral* during the GTGM-YTEC Geo01 and Geo02 campaigns in 2018. The hull-mounted parametric echosounder Parasound System DS3 (P70) with a fixed primary frequency of 22 kHz and a variable secondary low-frequency signal of 4 kHz was used. Acquisition was carried out using Teledyne's Parastore software. Boomer seismic data were acquired in 2009 during a joint campaign by IGeBA and OGS using a 150-J electrodynamic transducer (UWAK05 Nautik) and a 3 m single-channel streamer (array of 8 hydrophones) with a sampling rate of 50 µs and a recording length of 400 ms. Data were processed using Echos software (Paradigm®), following these processing steps: amplitude recovery (spherical divergence correction and inverse curve decay), time-varying filtering and spiking deconvolution. The seismic lines were interpreted using the software IHS Markit Kingdom®. A mean sound speed of 1500 m/s was assumed for the time-to-depth conversion of the interpreted horizons and the calculation of the isopach maps. The bathymetric and isopach grids, morphometric parameters, time series and wave height maps were produced using the free and open-source software QGIS GIS (http://www.qgis.org).

### 2.2 Tsunami modelling

An initial approach to analysing the tsunami potential of the recognized submarine MTDs was carried out using numerical modelling. The tsunami modelling includes three stages: (i) wave generation, (ii) propagation and (iii) inundation. Initial tsunami wave generation was introduced using the semi-empirical equations of Watts et al. (2005), which estimate the initial water surface disturbance that would result from a submerged sliding mass. This model assumes that the sliding mass is a solid rigid body with a length (b), width (w) and

thickness (T), moving along an inclined slope. The model assumes that most of the sea-level disturbance is generated during the initial acceleration phase and thus the effects due to deformation of the sliding mass are neglected (Watts et al. 2005; Løvholt et al. 2015).

The potential of a submarine landslide to trigger a tsunami depends on its volume, water depth and failure mechanism (Tappin 2010). In this work, the water depth and failure mechanism were assumed to be the same for all scenarios (T1 to T4). The pre-failure slab was assumed to have been located at the slope-break (Fig. 1), given the presence of sediment susceptible to fail in this area and that it constitutes the presumed provenance sector of the analysed MTDs. The submergence depth values are constrained by the numerical approach, where the condition $d/(b \sin \theta) > 0.5$ must be achieved (with d: submergence depth, b: length of the failed mass, θ: slope angle) to avoid part of the slide becoming subaerial (Watts et al. 2005), and by the basin floor (140 m bsl). In this case, a submergence depth of 70 m in present-day bathymetry conditions was chosen since it is the minimum value that fulfils the condition, and it is located at nearly the centre of the slope. While the failure mechanism was assumed to be translational rather than rotational, given the low thickness to run-out ratio (Mulder and Cochonat 1996), and the characteristics of the MTDs described later on in this work. The volumes for the different MTDs were estimated from the seismic data.

The resulting wave is calculated from a certain characteristic time ($t_0$) and travel distance ($S_0$) of the moving mass. The S0 corresponds to the length between the centre of the mass before and after the displacement (pre- and post-failure). Since we do not have neither multibeam nor seismic information about the MTD's scars, the geometrical parameters of the failed masses were estimated from the geometries measured from the deposits. The width was set equal to that of the slope-break, as this is the maximum width for a slab dethatching from this area. The length of the mass was estimated using the equation $S0 \sim 4.48b$ (Watts et al. 2005) and constrained by the extent of the glaciofluvial slope length. The thickness of the failed slab T was estimated volume using the following relationship: $V = b.w.T$, constrained by the thickness of glaciofluvial plain (with a maximum value of nearly 50 m) and by the average thickness of the deposits, measured in the seismic lines.

For the propagation phase, the open-source hydrodynamic model ANUGA was used (Nielsen et al. 2005; Roberts et al. 2015), which is written in Python and solves the non-linear shallow water equation (NLSWE) using a finite volume method. It uses the DE1 flow algorithm and has been validated with real cases and used to successfully model tsunami (Fernandes and Luis 2009; Jakeman et al. 2010; Wilson et al. 2018). However, this approach does not consider wave dispersion. In general, tsunami generated by landslides have smaller wavelength-to-depth ratios than earthquake tsunami, implying that frequency dispersion plays a role in wave generation and propagation (Glimsdal et al. 2013; Heidarzadeh et al. 2014; Løvholt et al. 2015). In this preliminary case, the dispersion effect was neglected for simplicity, as the parameters and elevation data used in this work are subject to several uncertainties, and only a small local area was included in the modelling. Simulations were run for a total time of 30 min for all scenarios with a time step of 10 s.

Although ANUGA successfully models the process of wetting and drying, when water inundates and retreats from coastal area, and this approach is therefore suitable for simulating tsunami inundation in coastal areas (Davies and Roberts 2015; Roberts et al. 2015), the coarse bathymetric and topographic grids (with cell sizes > 25 m) prevent the generation of accurate inundation maps and the calculation of realistic run-up heights. Therefore, the empirical formulas RUP1 of Ward and Asphaug (2003) and RUP2 Ward and Day (2008) were applied to estimate the potential run-up values, following the approach used

by previous authors (Brune et al. 2010a,b; Schwab et al. 2012; Lindhorst et al. 2014). For this purpose, a series of synthetic gauges were placed at the sites of interest (Fig. 1).

## 3 Subaqueous mass movements in Bahia Ushuaia

The sedimentary succession beneath the seafloor of Bahia Ushuaia is characterized by a ponded basin fill, with continuous sub-horizontal to SE dipping reflections that distally onlap against a bedrock high (Fig. 2). Within the stratified basin fill, several lenticular bodies with chaotic to semi-transparent acoustic facies are recognized. These deposits have the typical acoustic and morphological features that allow them to be interpreted as subaqueous mass transport deposits—MTDs (Moernaut and De Batist 2011). A total of eleven MTDs, labelled BU-A to BU-K (from the seabed downward), have been identified within the basin, interbedded with the stratified background sedimentation. The MTDs in Bahia Ushuaia vary in size, with four large deposits, several metres thick, located closer to the head of the basin. In this paper, the focus is on these four largest events (i.e. BU-A, BU-D, BU-G and BU-I), because of their larger size, better definition in the seismic data and greater importance in terms of the associated hazard, and they are also.

### 3.1 BU-I deposit

From bottom to top and from largest to smallest, the BU-I, is an extensive acoustically semi-transparent to chaotic body with ponded shape (Fig. 2). The irregular base scours deeply into the underlying layered reflections, indicating a highly erosive basal shear surface with several step-ups and step-downs (Figs. 2 and 3). The basal surface, alternately cutting older and younger strata, left some layered remnant blocks (Figs. 2 and 4C) and a rosary-shaped deposit in plain view (Fig. 5). Within the BU-I deposit, some internal SE-dipping reflections can be seen, indicating a rough stratification during downward transport (Figs. 2 and 4C). Distally, the deposit onlap against a glacial deposit attached to a bedrock high at the SE basin boundary, running slightly upwards over the opposing slope (Fig. 4A). Laterally, it onlaps against the steep flanks of the trough, which occupies the entire width of the basin. BU-I has an average thickness of 9 m, with two depocentres with thickness of up to 15 m in the proximal and central parts, decreasing distally. The deposit comprises a minimum volume of almost 57 million $m^3$ (Fig. 5). The run-out measured here from the toe of the slope to the furthest point of the deposit reaches 7.3 km. Stratigraphically on top of BU-I, there is a sheet-like body with semi-transparent acoustic internal fabric and a continuous sharp base with high amplitude (Figs. 2 and 4A). This layer has been interpreted as a cogenetic megaturbidite deposit (mt3). On the other hand, the bedrock below BU-I is characterized by a staircase morphology with some SE-dipping reflections and a normal fault affecting the layered basin fill (Figs. 2 and 4).

### 3.2 BU-G deposit

Nearly 8 m of sediment separates the top of mt3 from another large MTD (Fig. 2), referred to as BU-G. It has a wedge-shaped form, thickening towards the NW, and a chaotic to hummocky internal acoustic structure. Like BU-I, BU-G also has a strongly erosive base, but in this case consist of a main frontal ramp where the deposit steps-up from the basal shear surface and spreads across the palaeo-lakebed (Fig. 2). The frontal ramp is associated with

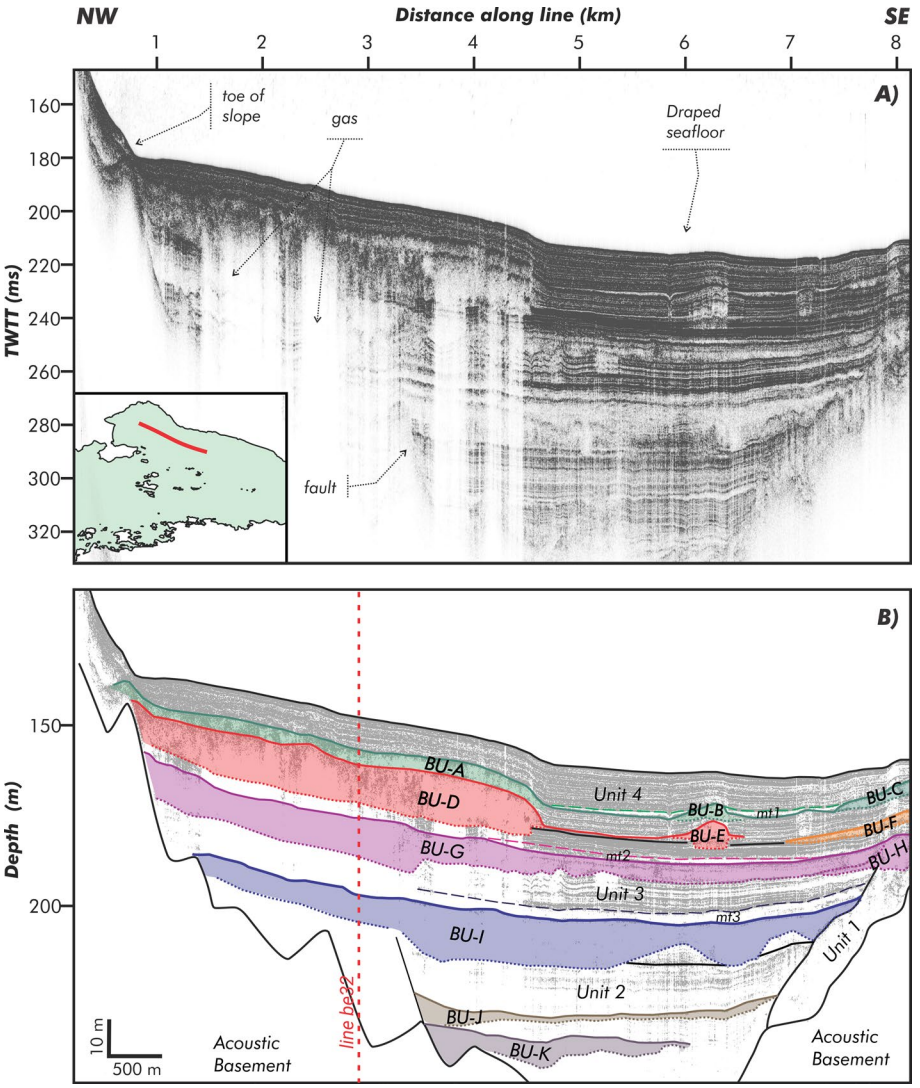


**Fig. 2** **A** Axial SBP line be-1333 along the Bahia-Ushuaia trough. **B** Interpreted line drawing. A series of stacked lenticular to wedge-shaped acoustically chaotic bodies are intercalated in the layered sedimentary sequence of the basin fill. The chaotic bodies correspond to mass transport deposits (top: solid line, bottom: dotted line), labelled BU-A to BU-K from top to bottom. Some semi-transparent tabular facies indicate megaturbidite deposits, represented by dashed lines and labelled mt1 to mt3. MTDs are present in seismic units interpreted as both lacustrine (units 2 and 3) and marine sediments (unit 4). Folded reflections can be observed beneath and in front of BU-G. Some of the MTDs can be laterally correlated, based on event horizons, and are therefore coloured the same. Note that BU-D acts as a seal for several vertical gas blow-out regions. The deep BU-J and BU-K are bounded by a fault that affects glaciolacustrine sediments and is associated with a steep slope. The acoustic foundation to the northwest is in the form of a staircase. The top of the slope, located at almost 150 m b.s.l., marks the transition from the glaciofluvial plain to the basin floor

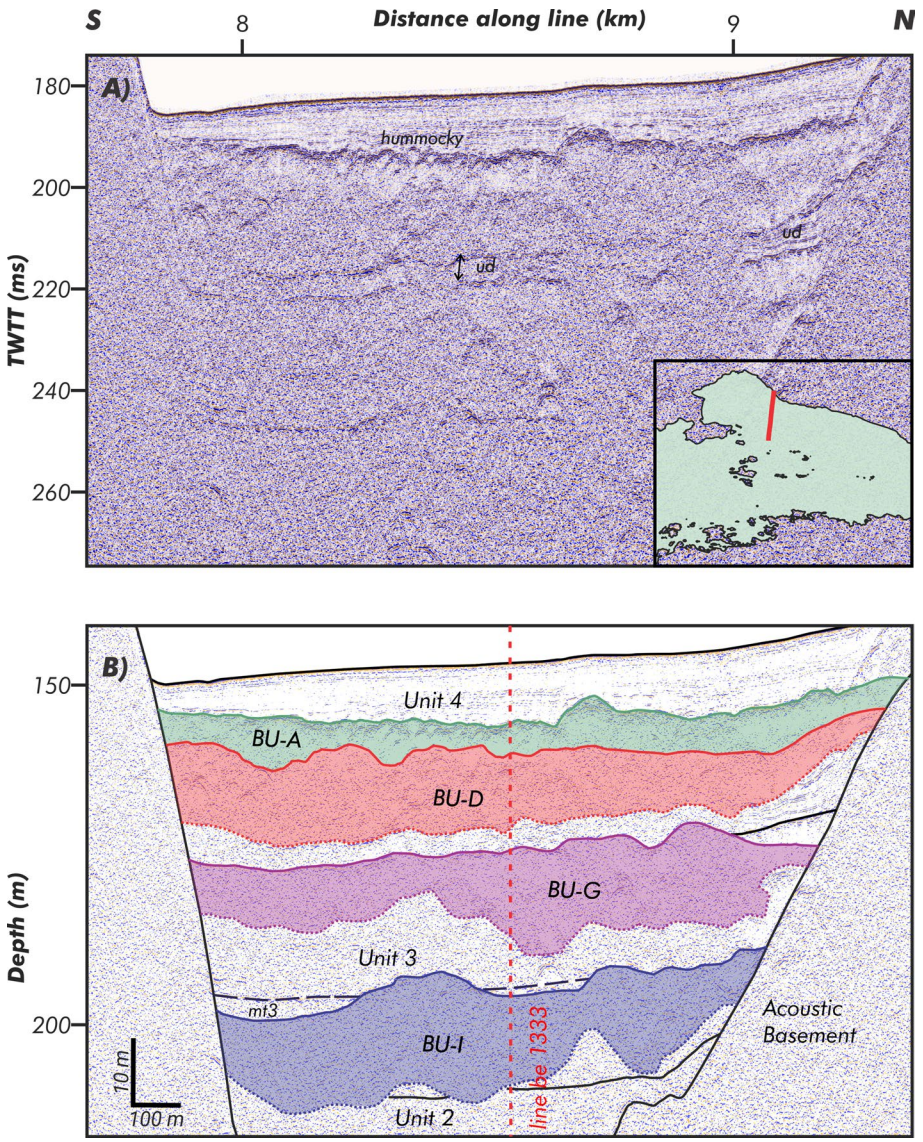


**Fig. 3** **A** Boomer seismic line be-32. **B** Interpreted line drawing. The stacked mass transport deposits onlap laterally against the steep and slightly asymmetric flanks of the trough. While the two deeper deposits (BU-I and BU-G) show very irregular erosive bases, the upper BU-A and BU-D show sharp conformable bases resting over a ~ 5 m thick tabular undisturbed deposit (ud). The top of BU-A shows a hummocky topography with several diffractions (d). The top layer of the deposit diverges to the north, indicating that the sediments are mainly derived from the delta systems at the head of the bay

contorted or wavy reflections in the footwall (Figs. 2 and 4). This possibly reflects a buttressing effect exerted by the emerging mass on the unconsolidated basin sediments. The wavy sediments are folded over a decoupling surface that appears to be on the same stratigraphic level as the initial BU-G basal shear surface (Fig. 4), suggesting a mechanically

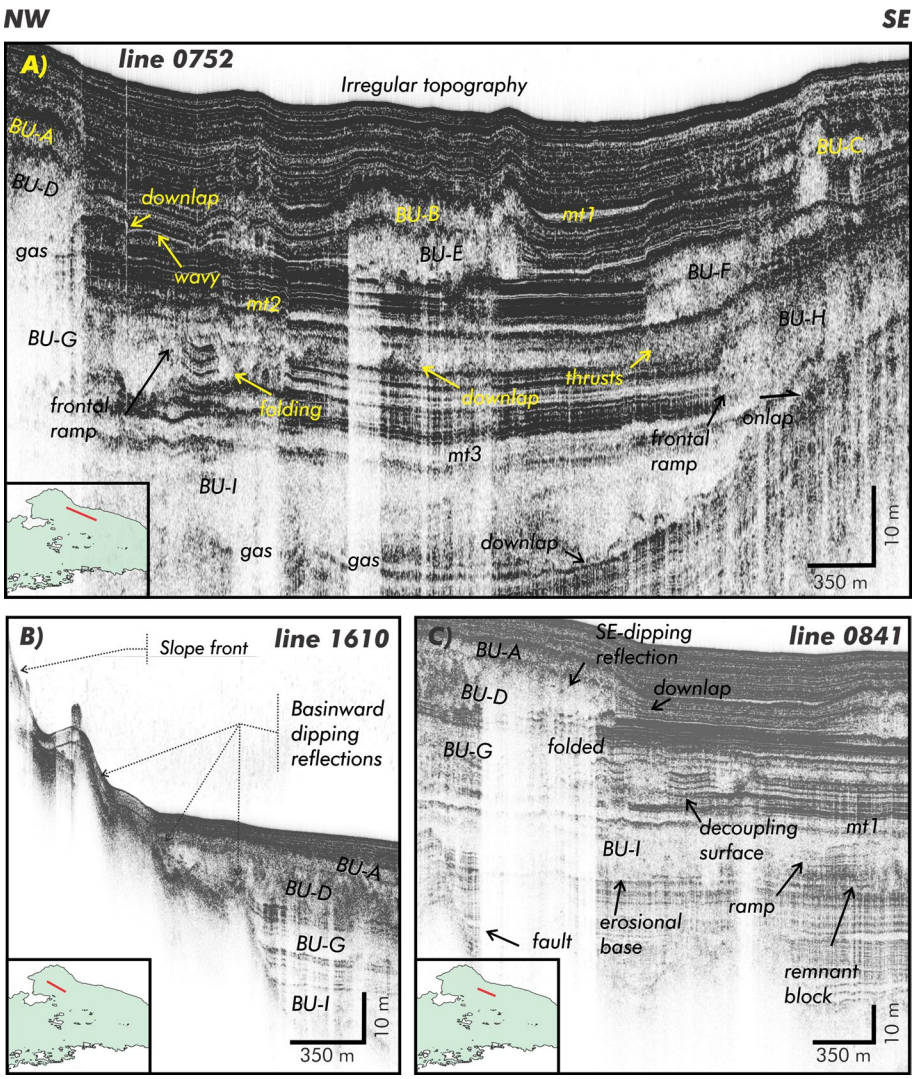


**Fig. 4** Detailed sections of SBP lines. **A** Section from line be-0752, zooming in on the northern part of the basin, showing the frontal segments of BU-A, -D, -G and -I. BU-G shows a frontal ramp associated with folding in the footwall. In front of BU-D the sediments are also slightly folded. The seabed shows irregular topography due to sediment draping of the underlying MTDs, in contrast to the smooth seabed above the undisturbed areas. **B** Section from line be-1610 in the proximal part of the basin. A series of basinward reflections is observed at the base of the slope-break. These features suggest the presence of discontinuities in the slope break, parallel to the fault recognized further east, that might have influenced the failure. **C** Section from line be-0841, zoom in on the central part of the basin. The frontal section of BU-I shows step-ups and -downs, leaving underlying remnant blocks with the unfailed stratified sediments. The megaturbidite deposit (mt3) covers the BU-I with a homogeneous thickness and a semi-transparent acoustic fabric. The buttressed deposits are located between BU-G and a decoupling surface. Further folded sediments are observed at BU-D. Within the glaciolacustrine deposits, below BU-I, a southeast-dipping normal fault is evident. This fault runs parallel to the steps observed in B

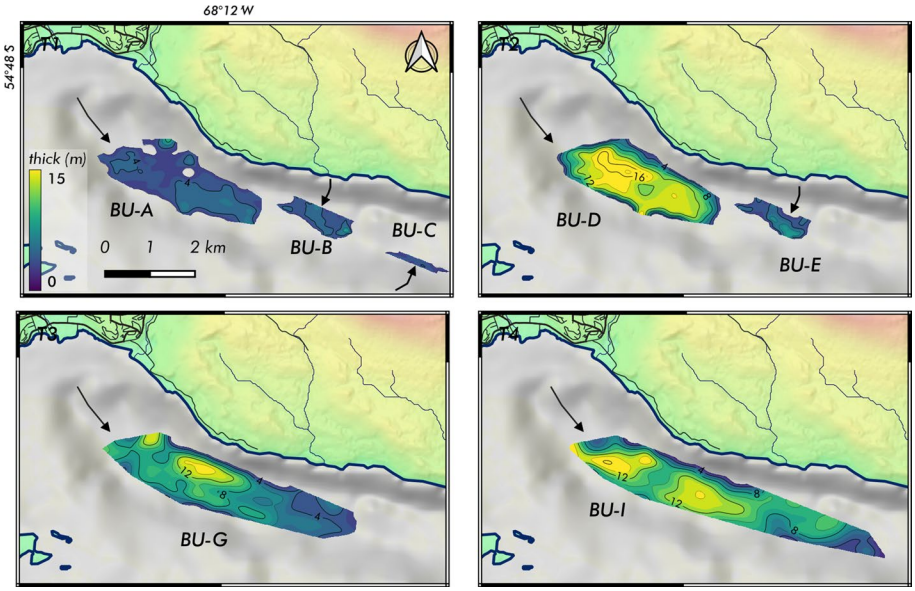


**Fig. 5** Isopach maps for the main recognized mass transport deposits of Bahia Ushuaia. Arrows indicate the provenance of each MTD

weak layer. The MTD is almost 6 km long and has an average thickness of 7 m, with the thickest part (12 m) in the proximal section, thinning towards the basin (Fig. 5). In cross-section, BU-G thickens towards the north (Fig. 3) laterally onlapping against the flanks and comprises a minimum volume of 48 million $m^3$. In the southeast, BU-G merges into another lens-shaped MTD (BU-H) (Figs. 2 and 4). Locally, BU-H overlies the BU-G deposit (Fig. 4A). In the thickest part of the BU-H deposit, some discontinuous SE-dipping reflections are observed, indicating that some degree of overthrusting has occurred. The deposits are overlain by a common high-amplitude reflection (Fig. 4) and were detached from a similar stratigraphic level before stepping up to the paleo-lakebed bed, namely the decoupling surface (Figs. 2 and 4A). Above BU-G and BU-H, there is a tabular, acoustically transparent layer with a sharp, non-erosive base, interpreted as a megaturbidite deposit (mt2, Fig. 2). The three large MTDs described so far (BU-I, BU-G and BU-H), and their associated megaturbidites deposits are contained within the seismic Unit 3 (ice-distal glaciolacustrine sediments) and can be thought of as having occurred during similar environmental conditions.

### 3.3 BU-D deposit

In the proximal section of the basin, stratigraphically above Unit 3, two large lenticular deposits stand out within the draping marine sediments of Unit 4: BU-D and BU-A (Fig. 2). Although these MTDs are smaller than those previously described, they comprise large volumes of sediment, BU-D being the largest of the two. BU-D is separated from the underlying BU-G by a layer of acoustically stratified sediments almost 4.5 m thick. The deposit has a lens shape with an undulating top, an opaque chaotic acoustic facies, an erosive basal shear zone and a convex front. What is interesting about the BU-D deposit

is that it is quite uniform in thickness (Fig. 2 & 4B), with an average of 10 m. Its length reaches almost 3.6 km, and it covers a total area of ~ 3.8 $km^2$ (Fig. 5). In total, it has mobilized almost 41 million $m^3$ of sediments downslope. In the frontal area, BU-D shows a small ramp marking the transition from the MTD to a metre-thick frontal turbidite deposit spread along the paleo-seafloor (Fig. 2). Wavy geometries are observed in some places in the sediments in front of BU-D, indicating local deformation (Fig. 4A). Some diffractions, especially in the frontal part of the deposit, indicate the presence of blocks (Fig. 4C). In the south-east, the BU-E deposit is on the same stratigraphic level as BU-D (Figs. 2 and 4), suggesting that they were deposited contemporaneously. In addition, some gas-blanking structures terminate at the BU-D deposit (Figs. 2 and 4C), suggesting that it served as a seal for fluid migration. It shows some upward and downward dipping internal reflections that seem to indicate shear surfaces within the deforming mass.

### 3.4 BU-A deposit

Directly overlying BU-D is BU-A, a lenticular, acoustically chaotic deposit with a similar extent than -D (~ 3.8 $km^2$), but with a much smaller thickness (~ 3.5 m) (Fig. 5). The total volume of sediments mobilized by the BU-A reaches 13 million $m^3$. The basal shear surface of BU-A is the top of the BU-D, meaning that the BU-A spread over the undulating topography resulted from the previous deposit, resulting in an irregular shape. BU-A is laterally correlated with the smaller MTDs BU-B and BU–C to the southeast by continuous top reflections of high amplitude (Figs. 2 and 4). The overlying sediments and the present-day seafloor show an undulating relief influenced by the MTDs at depth.

The provenance of the largest deposits (BU-I, BU-G, BU-D and BU-A) is thought to be in the NW, at the head of the bay, based on the NW-thickening of the deposits and the internal acoustic fabric and the presence of downlaps (Fig. 2). Although no clear signature of the source areas was evident in the seismic lines, the presence of basin ward steeply dipping reflections, the staircase-like morphology and the faults at the slope break, constitute elements that could have increase instability and control failure (Fig. 4B). On the other hand, the smaller, south-easterly MTDs were generated by events that failed from either the steep southern or northern flanks of the trough (Fig. 5).

### 3.5 Tsunami modelling

A numerical modelling was carried out as a first approximation to explore the tsunamigenic potential of the identified subaqueous mass movements. The hypothetical scenario assumes the occurrence of a subaqueous landslide in the present-day bathymetry of Bahia Ushuaia caused by a collapse at the front of the glaciofluvial slope (Fig. 1). The volumes of the slope failures for each scenario were approximated to those estimated for each of the MTD described in the previous section (Table 1): T1, T2, T3 and T4 associated to BU-A, BU-D, BU-G and BU-I, respectively. This provides an insight into the rupture scale required to trigger a potential tsunami in that sector of the trough.

### 3.6 Initial wave properties

Table 1 shows the modelling results for the four hypothetical landslide-triggered tsunami scenarios in Bahia Ushuaia. The initial 2D wave heights (η2D) for the T3-T4 scenarios

**Table 1** Input modelling parameters used for each scenario and calculated parameters of the generated landslides and initial waves

| | T1 | T2 | T3 | T4 |
|---|---|---|---|---|
| b (m) | 737 | 737 | 1004 | 1116 |
| w (m) | 1200 | 1200 | 1200 | 1200 |
| T (m) | 14 | 47 | 40 | 42 |
| d (m bsl) | 70 | 70 | 70 | 70 |
| V ($Mm^3$) | 12.61 | 41.45 | 48.46 | 56.80 |
| σ (°) | 7 | 7 | 7 | 7 |
| $S_0$ (m) | 3299.38 | 3299.76 | 4494.68 | 4996.07 |
| $t_0$ (s) | 96.24 | 96.24 | 112.33 | 118.43 |
| $v_0$ (m/s) | 34.28 | 34.28 | 40.01 | 42.19 |
| $a_0$ ($m/s^2$) | 0.36 | 0.36 | 0.36 | 0.36 |
| λ (m) | 2520.76 | 2520.76 | 2942.14 | 3101.91 |
| $\eta_{2D}$ (m) | 3.78 | 12.67 | 15.88 | 19.02 |
| $\eta_{3D}$ (m) | 1.21 | 4.09 | 4.60 | 5.31 |

*b* length of the sliding mass; *w* width of the sliding mass; *T* thickness of the sliding mass; *d* depth of the centre of mass of the mass before failure; *V*: volume of the sliding mass; *σ*: average slope value for the sliding plane; S0: characteristic sliding distance; t0: characteristic sliding time; v0: terminal velocity; a0: acceleration of the sliding mass; *λ* wavelength of the tsunami wave; η2D: initial wave height above the centre of mass; η3D: characteristic 3D tsunami amplitude above the landslide

give wave heights between 15 and 19 m above the centre of mass of the landslide with wavelength values close to 3 km. The T2 scenario associated with the BU-D event shows an initial tsunami wave with a height of 12.67 m and a wavelength of 2.5 km. The T1 scenario shows more conservative results with lower wave heights, but with the same wavelength, as the latter depends on the distance of the mass movement.

### 3.7 Tsunami propagation

The tsunami wave simulation shows maximum 3D heights (between 1 and 5 m) above the centre of mass of the failed mass and along coastlines, with a significant near-field effect (Fig. 6). While scenarios T2 to T4, associated with failures that generated the BU-D, BU-G and BU-I deposits, show potentially significant waves, especially in the coastal areas of Ushuaia (Fig. 6), scenario T1, which represents a failure with a volume similar to BU-A deposit, would produce waves of a few centimetres in size, barely noticeable on the shoreline. Wave propagation appears to be controlled by the Bridges archipelago; however, a positive sickled-shaped wave propagates in a south-westerly direction along a bathymetric depression between the Bridges and Eclaireurs Islands and along the northern shore of Ushuaia Trough (Fig. 7).

The first tsunami wave would have reached the entire central coastal region of BC within the first 15 min after the landslide. The arrival times of the first wave at the BC coast are similar for all scenarios, but only the time series for scenarios T4 and T2 are shown in Fig. 7, as these scenarios represent the events related to the largest deposit (BU-I) and the most recent large deposit (BU-D) with more realistic parameters (see discussion).

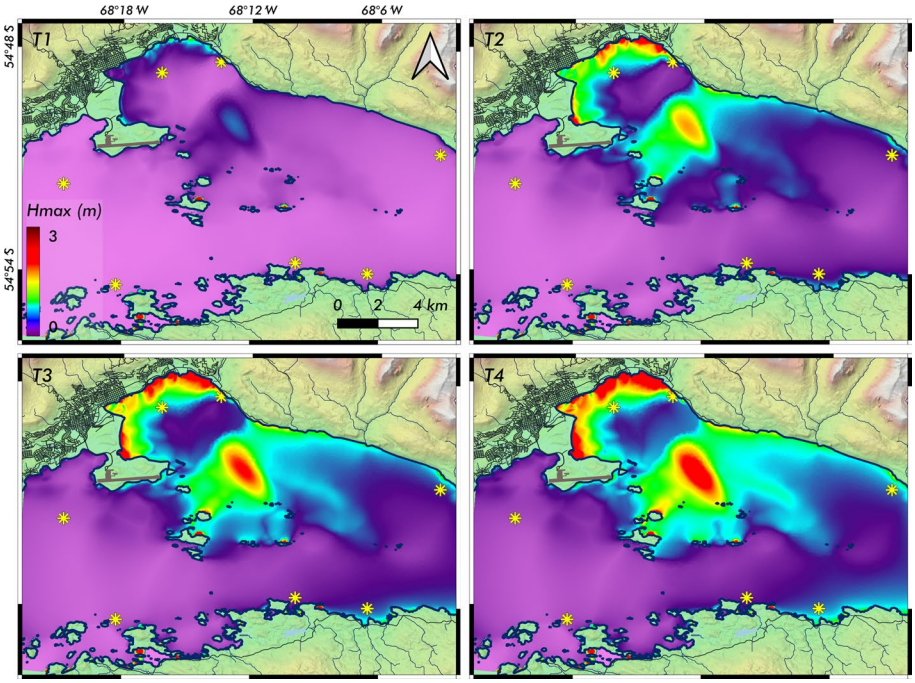


**Fig. 6** Maximum wave height (H max) after 30 min. The location of the synthetic gauges is shown in Fig. 1. T1, T2, T3 and T4 represent the different modelling scenarios, with sizes of the failed mass associated to BU-A, BU-D, BU-G and BU-I deposits, respectively

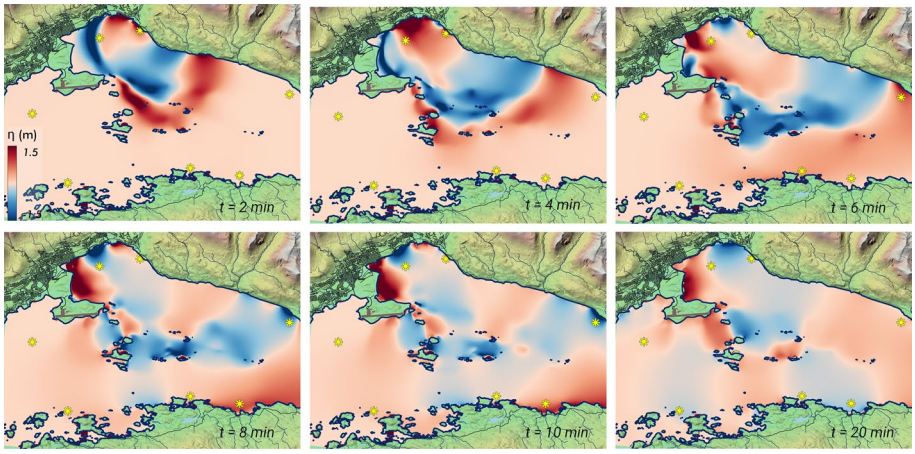


**Fig. 7** Timeseries of the simulated scenario for the BU-I failure over a time period of 20 min. The different maps depict the sea-level elevation or depression (stage η) at different intervals within the modelling time. The wave propagation after the initiation at Bahia Ushuaia, the arrival times and shapes at each gauge can be observed. Note the positive sickled-shaped front in a southwesterly direction. The Ushuaia shoreline is characterized by a leading depression followed by a nearly 2 m high offshore wave. For gauges labels refer to Fig. 1

At the head of the bay, an initial sea-level drop is followed by a 1–2-m-high positive wave that first hits Playa Larga with and moves anticlockwise along the shore (Fig. 7). This is also shown by the synthetic tide gauges in the port of Ushuaia and off Playa Larga (Fig. 8) with maximum heights of 1.3 and 0.70 m for T4 and T2, respectively. The gauges also show a series of trailing waves following the initial larger wave, probably due to reflections in the bay. The south-eastward wave propagates along the main axis of the trough towards Punta Segunda and reaches the main channel after 6 min. Off the coast of Punta Segunda, the maximum height of the wave generated is between 0.50 and 0.75 m for the scenarios related to the larger failures.

The southern and southwestern fronts propagate at a slower speed due to the shallower bathymetry determined by the bathymetric rise associated to Ushuaia Peninsula. On the southern Chilean coast, the wave would reach the Rosa site first, with a maximum offshore height of almost 0.40 m for scenario T4 and 0.3 m for T2. At the Mejillones gauge, on the other hand, the first arrival time is slightly delayed compared to Rosa, but has a greater

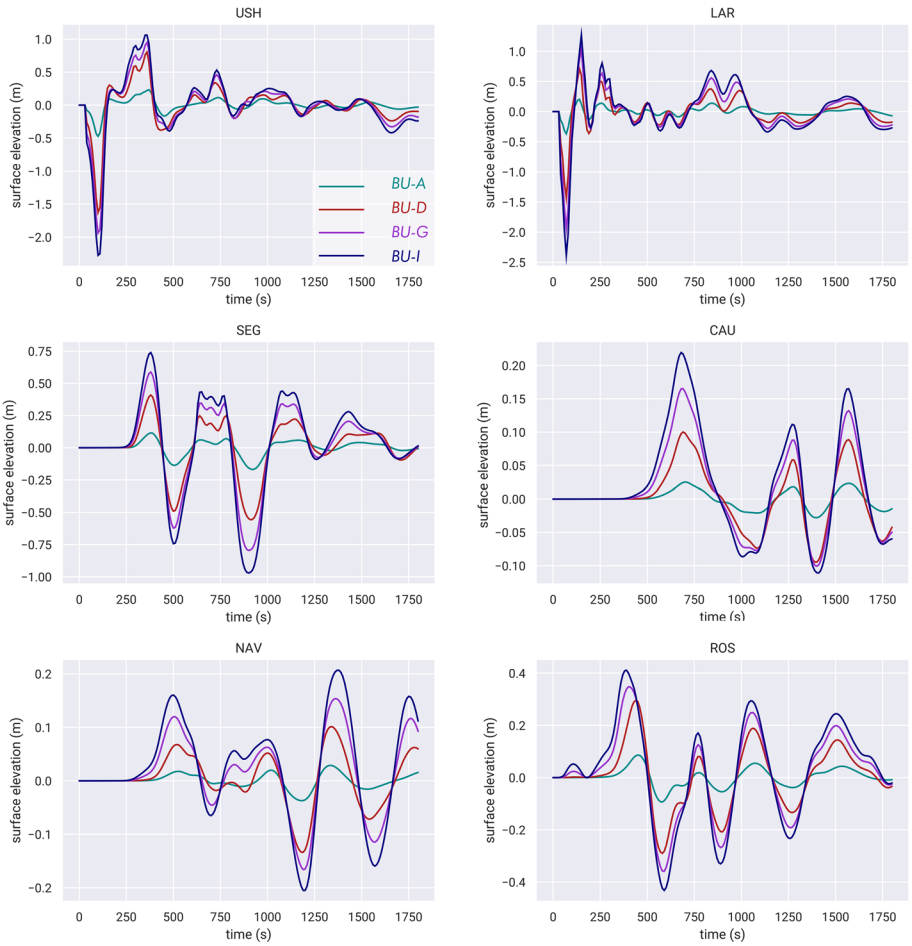


**Fig. 8** Time series (water level heights) at the locations corresponding to the synthetic gauges. The colours of the lines correspond to the individual MTDs events

height of almost 0.8 cm. Some trailing waves follow the first arrival with similar amplitudes. In Puerto Navarino, on the southern coast of BC, the first wave shows an estimated arrival time of 8 min with a maximum height of about 0.20 m. The third arrival wave shows a larger amplitude than the first. This could be related to resonance and wave amplification due to the morphology of the coast.

### 3.8 Estimated run-ups

A series of estimates for run-up values were made at selected sites. As the formula RUP2 (Ward and Day 2008) considers more parameters, it is assumed to provide a more realistic estimate of emergence than the simplified formula RUP1 (Ward and Asphaug 2003). The largest run-up heights, with values large enough to pose a hazard to coastal areas, are found at the Playa Larga and Punta Segunda gauges on the Argentine side and at the Mejillón gauging station on the Chilean coast, with run-up values > 7 m for scenario T4 and > 5 m for scenario T2 (Table 2). These locations are in the main direction of wave propagation and represent exposed coasts with steep offshore slopes. On the other hand, Ushuaia, Rosa and Navarino have moderate run-up heights, between 4 and 6 m for scenario T4.

In the event of a subaqueous landslide occurring on BU, the northern coastline of BC, from Ushuaia to Punta Segunda, shows the greatest potential tsunami hazard, with the greatest wave heights and run-ups, followed by the eastern half of the Chilean coast. The proximity to the tsunami source, the exposure to the tsunami wave propagation direction and the steep bathymetric slopes likely plays a critical role in determining the hazard. The locations in the western section of the central Beagle Channel have a lower potential tsunami hazard for a wave triggered in the BU, with the coastline west of the Ushuaia Peninsula having lower wave heights.

## 4 Discussion

### 4.1 Relative age and distribution

The results of this study confirm the role of gravitational processes as one of the most important sedimentary processes for the relocation of sediments from coastal areas to

**Table 2** Estimated Run-up values for selected locations, using the empirical equations of -RUP1- Ward and Asphaug (2003) and -RUP2- Ward and Day (2008)

| Gauge | $d$ (m b.s.l.) | $\sigma$ (°) | $H_{max}$(m) | | RUP1 (m) | | RUP2 (m) | |
|---|---|---|---|---|---|---|---|---|
| | | | BU-I | BU-D | BU-I | BU-D | BU-I | BU-D |
| ush | 28 | 1 | 1.06 | 0.78 | 2.04 | 1.6 | 4.54 | 3.84 |
| lar | 20 | 6 | 1.28 | 0.75 | 2.22 | 1.45 | 8.40 | 6.59 |
| seg | 31 | 4 | 0.75 | 0.41 | 1.58 | 0.98 | 7.38 | 5.62 |
| mej | 32 | 4 | 0.75 | 0.45 | 1.58 | 1.53 | 7.5 | 5.93 |
| ros | 31 | 6 | 0.41 | 0.29 | 0.98 | 0.74 | 6.82 | 5.82 |
| nav | 33 | 4 | 0.21 | 0.1 | 0.57 | 0.32 | 5.3 | 3.28 |
| cau | 20 | 1 | 0.22 | 0.1 | 1.16 | 0.29 | 1.95 | 1.36 |

deeper areas of Bahia Ushuaia within the BC, where these massive chaotic deposits are interbedded with the stratified background sedimentation. In fact, several post-glacial MTDs are found in the Bahia Ushuaia, some of which were of considerable dimensions, that have remobilised at least 170 million $m^3$ of sediments, constituting nearly a quarter of the basin fill, estimated in 676 million $m^3$. These deposits have similar acoustic characteristics (both SBP and boomer seismics) to other recurrent mass transport deposits documented in comparable fjord and lacustrine environments (e.g., Schnellmann et al. 2002; Bellwald et al. 2016; Wils et al. 2018).

The MTDs are distributed throughout the sedimentary sequence of BU and are interbedded within seismic units interpreted as background sediments from both glaciolacustrine (Units 2 and 3) and marine environments (Unit 4). Accordingly, the younger event deposits contained in Unit 4, such as BU-A and BU-D, occurred after the marine transgression, which took place in the early to mid-Holocene, *ca.* 8.5 cal kyr BP (Rabassa et al. 1986; Candel et al. 2018; McCulloch et al. 2019). On the other hand, the older and larger event deposits (e.g., BU-I and BU-G) are found between unconformities attributed to the top of glacial sediments and the base of the marine transgression. This places the oldest events between *ca.* 17 kyr and 8.5 kyr, a time when the central BC was ice-free under glaciolacustrine conditions (Rabassa et al. 2000; Hall et al. 2013; Candel et al. 2018; McCulloch et al. 2019). No recent mass transport deposits were observed along the present-day seafloor of Bahia Ushuaia.

The larger MTDs are found in the proximal section of the trough (Fig. 5). The location as well as the shape and acoustic properties of the deposits indicate that they originated as failures from the southeastern slope of the thick glaciofluvial plain at the head of the bay (Fig. 1), with a direction of movement towards the southeast. In this area, meltwater discharge from the Olivia and Grande rivers provided considerable amount of sediments susceptible to be remobilised and increased the slope load. Synsedimentary faults parallel to the slope break, as observed in the lowermost glaciolacustrine sediments, may have acted as preconditioning factors, suggesting that the failure could have initiated by creep (Mulder and Cochonat 1996; Fanetti et al. 2008) and ultimately triggered by an external factor.

On the other hand, the smaller deposits in the southeastern section of the trough (Fig. 4) originated as failures both the northern and southern flanks (Fig. 5) that may be associated with sidewall fan deltas fed by small tributaries reaching the trough from the north, or with the failure of hemipelagic sediment pockets deposited along the steep southern flank. It is possible to point out that the BU exhibits some form of MTD recurrence, at least following the deglaciation of the area, an aspect that is common in fjord head deltas (Stacey et al. 2018), where the failures occur under cyclic loading (e.g., Prior et al. 1986). The BU deposits are sandwiched between ~ 5 and 10-m thick packages of stratified sediments (Fig. 2).

### 4.2 Triggering

The largest BU-I deposit is located above a basin-wide unconformity, which becomes erosional towards the margins and that marks a significant change in the acoustic fabric between units 2 and 3. This change suggests an advance of coarser sandy/silty glaciofluvial-derived bottom currents, laterally associated with large incisions now observed as palaeochannels in the area (Bujalesky et al. 2004), over finer and thinner deposits. We interpret the occurrence of BU-I event during a drop in the lake level, which may have

conditioned slope stability in the basin. The BU-G deposit is also located within unit 3 and could also be associated with this environment.

As mentioned earlier, some MTDs share a common top horizon (Fig. 2), suggesting that these deposits likely result from coeval failures. This is the case at BU-A/B/C, BU-D/E and BU-G/H. The synchrony of some of the failures is also confirmed by the occurrence of megaturbidite deposits above the MTDs. Coeval slope failures are indicative of a regional trigger, usually an earthquake (Syvitski and Schafer 1996; Schnellmann et al. 2002; Praet et al. 2017; Wils et al 2018). However, also climatic events may trigger coeval slope failures (Tappin 2010). As the area is located near a plate boundary with moderate seismicity, with several historical high-magnitude earthquakes (Pelayo and Wiens 1989; Sabbione et al. 2007), it can be assumed that the above-mentioned coeval landslides were most likely triggered by seismic shaking. Moreover, recent findings of faulted deposits within the BC sediments, with ruptures younger than the marine transgression event (Bran et al. 2023), indicate that the channel is tectonically active, with deformation linked to the present-day transform plate boundary. This suggest that some of the MTDs events could have had a local seismic trigger. More data are needed however to link the slope failure events with specific source faults. The recognition and dating of recurrent synchronous MTDs provide a valuable opportunity for paleoseismological studies and seismic hazard assessment related to seismogenic structures on southern Patagonia (Waldmann et al. 2011; Wils et al 2018).

### 4.3 Classification and dynamics

Based on the acoustic architecture, motion and shape of slope failures, Mulder and Cochonat (1996) have proposed a classification for offshore mass movements. In general, an initial subdivision can be made between the older, pre-marine transgression (BU-I and -G) and the Holocene deposits (BU-A and -D), as they differ in shape, degree of erosion and internal acoustic structure. These differences suggest different movement dynamics and/or sediment properties. The older BU-I shows a highly eroded basal surface and appears as a highly disaggregated deposit, as evidenced by the internal downward dipping reflections and the ponded shape with distally onlapping reflections. Basal scouring in BU-I, extending almost 8 m into the underlying deposits, indicates a violent, high-energy event. Together with the semi-transparent to chaotic acoustic fabric, indicating matrix-supported deposition, this led to the interpretation of the BU-I as originated from a non-cohesive debris flow. However, for the BU-G, it is possible to interpret an initial frontally confined (Moernaut and De Batist 2011) slide phase that exerted a buttressing effect on the basin floor sediments, which resulted in local folding. The slide later transitioned into a highly mobile debris flow that emerged frontally and spilled over the contemporaneous basin floor. We interpret that both events involved poorly consolidated sandy-silty glacial or glaciofluvial sediments that resulted in long ($\geq$6 km) ponded acoustically chaotic deposits. Moreover, basal erosion implies that the MTD events reworked and incorporated basin-floor sediments during movement, implying that the calculated final volume of deposits might overestimate the initial evacuation volume (e.g., Prior et al. 1984; Hilbe and Anselmetti 2014).

On the other hand, the lenticular BU-A and-D deposits are less erosive, have frontally emerging sharp bases, homogeneous thickness and steep convex fronts. These features indicate lower energy at the base of the events and a higher degree of cohesion within the sediment than in the older events. We interpret these deposits as the result of failures

with translational movement along a defined basal shear surface. In both cases, these are frontally emerging slides that have different volumes but similar lengths, suggesting that sediment properties may have controlled their propagation into the basin rather than the size of the failure. In addition, the opaque chaotic acoustic fabric, which has higher amplitudes than the older deposits, suggests a higher clay content. This fits with environmental changes in the Beagle area during the early to mid-Holocene, which include the establishment of a marine environment, but also a wetter climate with an increase in vegetation cover and the recession of glaciers into the inner cirques (Menounos et al. 2013; Candel and Borromei 2016; Candel et al. 2018). Similar results are described by Lowag et al. (2012) in the post-glacial sedimentary record of Windermere Lake, where MTDs were associated with the Younger Dryas deterioration event, which involved higher mobility and less consolidated deposits compared to Holocene mass transport deposits. This illustrates how climatic controls on erosion and denudation within the catchment influence the sediment budget during source-to-sink depositional processes, which ultimately translates into different types of mass movements as observed in Bahia Ushuaia.

### 4.4 Tsunamigenic potential

One of the most important effects of subaqueous mass movements is their capacity to generate tsunami waves, and thus their potential threat to coastal communities near the failure zone. The results presented in this paper are preliminary and should be considered as a first approximation, as the modelling approach and the lack of accurate bathymetric and seismic data from the slope areas where the MTDs originated from carry several limitations. The largest initial waves occur in the T3 and T4 scenarios, with values of more than 15 m. However, the initial wave is largely dependent on the volume of the failed mass (Brune et al. 2010a,b; Tappin 2010), so overestimating this volume in the calculation could result in a higher wave. Another important factor controlling the height of the initial wave is the failure submergence depth (Tappin 2010; Grilli and Watts 2005). In this case, however, there is a constraint imposed by the numerical approach, resulting in a potential underestimation of the wave height, given that shallower failures are likely to generate hazardous waves. Although wave height is assumed to be determined mainly by the initial acceleration phase (Watts et al. 2005; Løvholt et al. 2015), the MTDs studied in this paper show several signs of deformation, particularly the oldest deposits that have been interpreted as originated from debris flows, or at least have transitioned into this type of movement involving disaggregation. Therefore, a fixed-rigid approach would involve some inaccuracies that could lead to an overestimation of the resulting wave height. All in all, the values obtained for the T1 and T2 scenarios are considered more realistic than the values for older events.

Nevertheless, the results indicate that at least three of the investigated deposits in Bahia Ushuaia resulted from events that had the potential to generate local hazardous tsunami waves. The resulting local wave heights are comparable to real and modelling cases of tsunami related to submarine landslides in fjords and lakes (e.g., Watts et al. 2003; Lindhorst et al. 2014). The thick megaturbidite deposits over the MTDs are another indication of the possible generation of tsunami waves associated with the largest failures at BU. Megaturbidites are formed by the deposition of suspension plumes resulting from large submarine landslides and associated tsunami and seiche waves (Schnellmann et al. 2005; Waldmann et al. 2011).

Historical tsunami events have been mentioned in Tierra del Fuego along the coast of the Strait of Magellan (Lomnitz 1970) after the Mw 7.5 and 7.75 earthquakes of 1949 (Lomnitz 1970; Pelayo and Wiens 1989). However, tsunamigenic deposits are rare in Tierra del Fuego, with only a single Holocene event deposit reported from the Atlantic coast of Tierra del Fuego (Bujalesky 2012), possibly related to an earthquake-triggered tsunami on the Scotia Arc (Dragani et al. 2009; Bujalesky 2012). No direct evidence of a tsunami has yet been found in the Beagle Channel. A number of elevated marine sediments have been found at several locations along the southern and northern BC coast (Gordillo et al. 1992; McCulloch et al. 2019; Bjoerck et al., 2021), corresponding to elevated palaeocoastlines. Nevertheless, the tsunamigenic significance, at least for some of the sites along the BC, has not been thoroughly investigated. Ancient oral tales of the region's native people, the Yahganes, refer to a catastrophic flooding episode that may be related to the occurrence of a tsunami in the Beagle Channel (Isla and Bujalesky 2004). Settlement of the southern Fuegian archipelago by early humans would have begun during the early Holocene (Zangrando et al. 2018), spanning a time interval that makes it possible for the story to be rooted in one of the Holocene mass transport deposits recognized at Bahia Ushuaia. Further research should therefore be conducted to investigate the occurrence of past tsunami in the Fuegian archipelago. In addition, more data are needed to better constrain the modelling parameters, in particular high-resolution topographic and bathymetric grids and a more sophisticated modelling approach, especially including a deforming mass during initial formation and dispersive effects during propagation (Heidarzadeh et al. 2014), to make an accurate assessment of the landslide-induced tsunami hazard in the Beagle Channel.

## 5 Conclusions

A series of subaqueous MTDs have been identified within the post-glacial sedimentary succession of central Beagle Channel. The basin fill shows a recurrence of large MTDs that involves individual minimum volumes up to 57 million $m^3$, and a total volume of remobilised sediments ranging 170 million $m^3$. This constitutes a quarter of the total basin fill. Using seismic data, it is possible to differentiate between highly disintegrative Pleistocene to early Holocene erosive flows and shorter more cohesive Holocene deposits.

The large MTDs were derived from failures of the thick glaciofluvial deposits located at the head of Bahia Ushuaia and are associated with up to 10 m thick megaturbidite deposits. In this area, sediment loading is controlled by the meltwater discharge of Olivia and Grande rivers. Smaller events originated from side-wall tributary deltas and hemipelagic slope sediments. Most of the mass movement deposits bear evidence of having been triggered by earthquakes associated to the transform plate boundary, with possible local sources. This work reveals that the Beagle Channel is highly prone to large subaqueous mass movement events and more research should carried out within the channel, considering areas with failure recurrence or sectors with unstable sediments susceptible to collapse.

In addition, a preliminary analysis of potential tsunami wave generation associated with the largest subaqueous failures were carried out using numerical modelling. Results suggest that at least three of them would have the potential to generate hazardous waves with maximum heights that can reach up to 1–2 m in the Ushuaia's harbour, with estimated run-up heights ranging from 2 to 8 m. Although the numerical modelling approach employed in this work carries several limitations, it constitutes a benchmark for tsunami hazard assessment in the area. Further detailed analysis is recommended,

especially regarding a more sophisticated modelling and a refinement of the bathymetric and topographic data resolution for strategic areas.

**Acknowledgements** This contribution is framed within a collaboration between the National Scientific and Technical Research Council (CONICET – MINCyT) and YPF technology S.A. (Y-TEC). In particularly the data presented in this manuscript were partly acquired on board the R/V Austral in the cruise YTEC-GTGM 2. In addition, this work was partly funded by the PiP CONICET 2021-2023 (11220200103152CO). "Estudio sismoacústico y morfosedimentario del margen continental argentino (sectores patagónico y bonaerense meridional). Interacción de procesos endógenos y exógenos. (SIMOCA). We thank Marc DeBatist for his constructive that have largely improve the original manuscript. We ackowledge J.L. Hormaechea, G. Connon, L. Barbero and C. Ferrer of the Estación Astronómica de Río Grande (EARG) and Horacio Lippai (IGeBA) for their support during data acquisition in the field. We acknowledge the Servicio de Hidrografía Naval (SHN; Argentine Hydrographic Survey) and the captain, officials and crew of the R/V Austral.

**Author contributions** All authors contributed to the study conception and design. Material preparation, data collection and analysis were performed by AT, EL, DMB and JGL. Conceptualization by DMB and FP. Numerical modelling was performed by DMB and SP. Funding and project administration led by AT. The first draft of the manuscript was written by DMB, and all authors commented on previous versions of the manuscript. All authors read and approved the final manuscript.

**Funding** This work was supported by the project YTEC-GTGM. This work was partly funded by the PiP CONICET 2021–2023 (11220200103152CO). "Estudio sismoacústico y morfosedimentario del margen continental argentino (sectores patagónico y bonaerense meridional). Interacción de procesos endógenos y exógenos. (SIMOCA). Part of the funding for the acquisition of high-resolution seismic data comes from a bilateral project between Italy and Argentina, financed by the Italian Ministry of Foreign Affairs (MAE).

## Declarations

**Conflict of interest** The authors have no relevant financial or non-financial interests to disclose.

## References

Bellwald B, Hjelstuen BO, Sejrup HP, Stokowy T, Kuvås J, (2019) Holocene mass movements in west and mid-Norwegian fjords and lakes. Marine Geology

Bellwald B, Hjelstuen BO, Sejrup HP, Haflidason H (2016) Postglacial mass movements and depositional environments in a high-latitude fjord system: Hardangerfjorden, Western Norway. Mar Geol 379:157–175. https://doi.org/10.1016/j.margeo.2016.06.002

Björck S, Lambeck K, Möller P, Waldmann N, Bennike O, Jiang H, Li D, Sandgren P, Nielsen AB, Porter CT (2021) Relative sea level changes and glacio-isostatic modelling in the Beagle Channel, Tierra del Fuego, Chile: glacial and tectonic implications. Quat Sci Rev 251:106657

Boyd BL, Anderson JB, Wellner JS, Fernandez RA (2008) The sedimentary record of glacial retreat, Marinelli Fjord, Patagonia: regional correlations and climate ties. Mar Geol 255:165–178

Bran DM, Palma F, Menichetti M, Lodolo E, Bunicontro S, Lozano JG, Baradello L, Winocur D, Grossi M, Tassone AA (2023) Active faulting in the Beagle Channel (Tierra del Fuego). Terra Nova. https://doi.org/10.1111/ter.12658

Brune S, Babeyko AY, Ladage S, Sobolev SV (2010a) Landslide tsunami hazard in the Indonesian Sunda Arc. Nat Hazard 10:589–604. https://doi.org/10.5194/nhess-10-589-2010

Brune S, Babeyko AY, Müller C, Kopp H, Sobolev SV (2010b) Submarine landslides at the eastern Sunda margin: observations and tsunami impact assessment. Nat Hazards 54:547–562. https://doi.org/10.1007/s11069-009-9487-8

Bujalesky G, Aliotta S, Isla F (2004) Facies del subfondo del canal Beagle, Tierra del Fuego. Revista De La Asociación Geológica Argentina 59:29–37

Bujalesky GG (2012) Tsunami overtopping fan and erosive scarps at Atlantic coast of Tierra del Fuego. J Coastal Res 28:442–456

Bujalesky GG, (2011) The flood of the Beagle Valley (11.000 YR BP), Tierra del Fuego. In: Anales Del Instituto de La Patagonia. pp. 5–21

Bujalesky GG (2007) Coastal geomorphology and evolution of Tierra del Fuego (Southern Argentina). Geologica Acta 5:337–362

Candel MS, Borromei AM, (2016) Review of the palaeoenvironmental reconstruction of Late Quaternary marine sequences, Tierra del Fuego (Argentina). Publicación Electrónica de la Asociación Paleontológica Argentina 16

Candel MS, Borromei AM, Louwye S (2018) Early to middle Holocene palaeoenvironmental reconstruction of the Beagle Channel (southernmost Argentina) based on terrestrial and marine palynomorphs. Boreas 47:1072–1083. https://doi.org/10.1111/bor.12322

Connon, G.C., Bollini, M.C., Sabbione, N.C., Hormaechea, J.L., 2021. Complemento 2017–2020 del Catálogo Sismológico de Referencia de Tierra del Fuego.

Davies G, Roberts S, (2015) Open source flood simulation with a 2D discontinuous-elevation hydrodynamic model. In: Proceedings of MODSIM 2015

De Batist M, Talling P, Strasser M, Girardclos S (2017) Subaquatic paleoseismology: records of large Holocene earthquakes in marine and lacustrine sediments. Mar Geol 384:1–3. https://doi.org/10.1016/j.margeo.2017.04.010

Dragani WC, D'Onofrio EE, Grismeyer W, Fiore MM, Violante RA, Rovere EI (2009) Vulnerability of the Atlantic Patagonian coast to tsunamis generated by submarine earthquakes located in the Scotia Arc region. Some Numer Exp Nat Hazards 49:437–458

Esteban F, Bran DM, Tassone A, Menichetti M, Lodolo E, Lippai H, Vilas JF (2013) The structures of the Peninsula Ushuaia in the Beagle Channel (Tierra del Fuego, Argentina). Rendiconti Online Societa Geologica Italiana 29:43–36

Fanetti D, Anselmetti FS, Chapron E, Sturm M, Vezzoli L (2008) Megaturbidite deposits in the Holocene basin fill of Lake Como (southern Alps, Italy). Palaeogeogr Palaeoclimatol Palaeoecol 259:323–340

Fernandes M, Luis J, (2009) Comparing shallow water numerical models AnuGA and COMCOT for tsunami propagation and inundation at bay of Alvor, south of Portugal. 412

Fernández R, Gulick S, Rodrigo C, Domack E, Leventer A (2017) Seismic stratigraphy and glacial cycles in the inland passages of the Magallanes Region of Chile, southernmost South America. Mar Geol 386:19–31. https://doi.org/10.1016/j.margeo.2017.02.006

Glimsdal S, Pedersen GK, Harbitz CB, Løvholt F (2013) Dispersion of tsunamis: does it really matter? Nat Hazard 13:1507–1526. https://doi.org/10.5194/nhess-13-1507-2013

Gordillo S, Bujalesky GG, Pirazzoli PA, Rabassa JO, Saliège J-F (1992) Holocene raised beaches along the northern coast of the Beagle Channel, Tierra del Fuego, Argentina. Palaeogeogr Palaeoclimatol Palaeoecol 99:41–54. https://doi.org/10.1016/0031-0182(92)90006-Q

Grilli ST, Watts P (2005) Tsunami generation by submarine mass failure. I: modeling, experimental validation, and sensitivity analyses. J Waterw Port Coast Ocean Eng 131:283–297. https://doi.org/10.1061/(ASCE)0733-950X(2005)131:6(283)

Hall BL, Porter CT, Denton GH, Lowell TV, Bromley GR (2013) Extensive recession of Cordillera Darwin glaciers in southernmost South America during Heinrich stadial 1. Quat Sci Rev 62:49–55

Hampton MA, Lee HJ, Locat J (1996) Submarine landslides. Rev Geophys 34:33–59. https://doi.org/10.1029/95RG03287

Harbitz CB, Løvholt F, Bungum H (2014) Submarine landslide tsunamis: how extreme and how likely? Nat Hazards 72:1341–1374. https://doi.org/10.1007/s11069-013-0681-3

Heidarzadeh M, Krastel S, Yalciner AC, (2014) The state-of-the-art numerical tools for modeling landslide tsunamis: a short review. In: Krastel S, Behrmann JH, Völker D, Stipp M, Berndt C, Urgeles R, Chaytor J, Huhn K, Strasser M, Harbitz CB (Eds), Submarine mass movements and their consequences: 6th international symposium, advances in natural and technological hazards research. Springer International Publishing, Cham, pp. 483–495. Doi: https://doi.org/10.1007/978-3-319-00972-8_43

Heusser CJ (1993) Late-glacial of southern South America. Quat Sci Rev 12:345–350

Hilbe M, Anselmetti FS (2014) Signatures of slope failures and river-delta collapses in a perialpine lake (Lake Lucerne, Switzerland). Sedimentology 61:1883–1907. https://doi.org/10.1111/sed.12120

Isla F, Bujalesky G, Coronato A (1999) Procesos estuarinos en el canal Beagle, Tierra del Fuego. Revista De La Asociación Geológica Argentina 54:307–318

Isla FI, Bujalesky GG (2004) El Maremoto De Los Yaganes. Nexos 11:29–33

Jakeman JD, Nielsen OM, Putten KV, Mleczko R, Burbidge D, Horspool N (2010) Towards spatially distributed quantitative assessment of tsunami inundation models. Ocean Dyn 60:1115–1138

Lindhorst K, Krastel S, Papenberg C, Heidarzadeh M, (2014) Modeling submarine landslide-generated waves in Lake Ohrid, Macedonia/Albania. In: submarine mass movements and their consequences. Springer, pp. 497–506

Lodolo E, Menichetti M, Bartole R, Ben-Avraham Z, Tassone A, Lippai H, (2003) Magallanes-Fagnano continental transform fault (Tierra del Fuego, southernmost South America). Tectonics 22

Lomnitz C (1970) Major earthquakes and tsunamis in Chile during the period 1535 to 1955. Geol Rundsch 59:938–960

Løvholt F, Pedersen G, Harbitz CB, Glimsdal S, Kim J (2015) On the characteristics of landslide tsunamis. Philos Trans R Soc Math Phys Eng Sci 373:20140376

Lowag J, Bull JM, Vardy ME, Miller H, Pinson LJW (2012) High-resolution seismic imaging of a Younger Dryas and Holocene mass movement complex in glacial lake Windermere, UK. Geomorphology 171–172:42–57. https://doi.org/10.1016/j.geomorph.2012.05.002

Masson DG, Harbitz CB, Wynn RB, Pedersen G, Løvholt F (2006) Submarine landslides: processes, triggers and hazard prediction. Philos Trans R Soc Math Phys Eng Sci 364:2009–2203

McCulloch RD, Blaikie J, Jacob B, Mansilla CA, Morello F, De Pol-Holz R, San Román M, Tisdall E, Torres J (2020) Late glacial and Holocene climate variability, southernmost Patagonia. Quat Sci Rev 229:106131

McCulloch RD, Mansilla CA, Morello F, De Pol-Holz R, San Roman M, Tisdall E, Torres J (2019) Late glacial and Holocene landscape change and rapid climate and coastal impacts in the Canal Beagle, southernmost Patagonia. J Quat Sci 34:674–684

Menichetti M, Lodolo E, Tassone A (2008) Structural geology of the Fuegian Andes and Magallanes fold-and-thrust belt-Tierra del Fuego Island. Geol Acta 6:19–42

Menounos B, Clague JJ, Osborn G, Davis PT, Ponce F, Goehring B, Maurer M, Rabassa J, Coronato A, Marr R (2013) Latest Pleistocene and Holocene glacier fluctuations in southernmost Tierra del Fuego, Argentina. Quat Sci Rev 77:70–79

Moernaut J, De Batist M (2011) Frontal emplacement and mobility of sublacustrine landslides: results from morphometric and seismostratigraphic analysis. Mar Geol 285:29–45. https://doi.org/10.1016/j.margeo.2011.05.001

Mulder T, Cochonat P (1996) Classification of offshore mass movements. J Sediment Res 66:43–57. https://doi.org/10.1306/D42682AC-2B26-11D7-8648000102C1865D

Nielsen O, Roberts S, Gray D, McPherson A, Hitchman A, (2005) Hydrodymamic modelling of coastal inundation. In: MODSIM 2005 international congress on modelling and simulation, pp 518–523

Pelayo AM, Wiens DA (1989) Seismotectonics and relative plate motions in the Scotia Sea region. J Geophys Res Solid Earth 94:7293–7320

Praet N, Moernaut J, Van Daele M, Boes E, Haeussler PJ, Strupler M, Schmidt S, Loso MG, De Batist M (2017) Paleoseismic potential of sublacustrine landslide records in a high-seismicity setting (south-central Alaska). Mar Geol 384:103–119. https://doi.org/10.1016/j.margeo.2016.05.004

Prior DB, Bornhold BD, Johns MW (1984) Depositional Characteristics of a Submarine Debris Flow. J Geol 92:707–727. https://doi.org/10.1086/628907

Prior DB, Yang Z-S, Bornhold BD, Keller GH, Lu Z, Wiseman WJ Jr, Wright LD, Zhang J (1986) Active slope failure, sediment collapse, and silt flows of the modern subaqueous Huanghe (Yellow River) delta. Geo Mar Lett 6:85–95

Rabassa J, Coronato A, Bujalesky G, Salemme M, Roig C, Meglioli A, Heusser C, Gordillo S, Roig F, Borromei A (2000) Quaternary of Tierra del Fuego, southernmost South America: an updated review. Quat Int 68:217–240

Rabassa J, Coronato A, Martinez O (2011) Late Cenozoic glaciations in Patagonia and Tierra del Fuego: an updated review. Biol J Lin Soc 103:316–335

Rabassa J, Heusser C, Stuckenrath R, (1986) New data on Holocene sea transgression in the Beagle Channel: Tierra del Fuego, Argentina. In: International symposium on sea-level changes and quaternary shorelines. pp 291–309

Roberts S, Nielsen O, Gray D, Sexton J, Davies G (2015). ANUGA user manual (manual)

Sabbione N, Connon G, Bufón C, Hormaechea, J, (2007) Tierra del Fuego reference standard earthquake catalogue. In: Geosur 2007, Congreso Internacional Sobre Geologıa y Geofısica Del Hemisferio Sur (Santiago de Chile), p. 143

Schnellmann M, Anselmetti FS, Giardini D, McKENZIE JA (2005) Mass movement-induced fold-and-thrust belt structures in unconsolidated sediments in Lake Lucerne (Switzerland). Sedimentology 52:271–289. https://doi.org/10.1111/j.1365-3091.2004.00694.x

Schnellmann M, Anselmetti FS, Giardini D, McKenzie JA, Ward SN (2002) Prehistoric earthquake history revealed by lacustrine slump deposits. Geology 30:1131–1134

Schwab JM, Krastel S, Grün M, Gross F, Pananont P, Jintasaeranee P, Bunsomboonsakul S, Weinrebe W, Winkelmann D (2012) Submarine mass wasting and associated tsunami risk offshore western Thailand, Andaman Sea, Indian Ocean. Nat Hazard 12:2609–2630. https://doi.org/10.5194/nhess-12-2609-2012

Stacey CD, Lintern DG, Enkin RJ (2018) Multifaceted re-analysis of the enigmatic Kitimat slide complex, Canada. Sed Geol 369:46–59. https://doi.org/10.1016/j.sedgeo.2018.01.006

St-Onge G, Chapron E, Mulsow S, Salas M, Viel M, Debret M, Foucher A, Mulder T, Winiarski T, Desmet M (2012) Comparison of earthquake-triggered turbidites from the Saguenay (Eastern Canada) and Reloncavi (Chilean margin) Fjords: implications for paleoseismicity and sedimentology. Sed Geol 243:89–107

Syvitski JP, Burrell DC, Skei JM (1987) Fjords processes and products, 1st edn. Springer

Syvitski JPM, Schafer CT (1996) Evidence for an earthquake-triggered basin collapse in Saguenay Fjord, Canada. Sediment Geol Mar Sediment Events Rec 104:127–153. https://doi.org/10.1016/0037-0738(95)00125-5

Tappin DR (2010) Submarine mass failures as tsunami sources: their climate control. Philos Trans R Soc Math Phys Eng Sci 368:2417–2434

Waldmann N, Anselmetti FS, Ariztegui D, Austin JA Jr, Pirouz M, Moy CM, Dunbar R (2011) Holocene mass-wasting events in Lago Fagnano, Tierra del Fuego (54°S): implications for paleoseismicity of the Magallanes-Fagnano transform fault: Holocene mass-wasting events in Lago Fagnano, Tierra del Fuego (54°S). Basin Res 23:171–190. https://doi.org/10.1111/j.1365-2117.2010.00489.x

Ward SN, Asphaug E (2003) Asteroid impact tsunami of 2880 March 16. Geophys J Int 153:F6–F10. https://doi.org/10.1046/j.1365-246X.2003.01944.x

Ward SN, Day S (2008) Tsunami balls: a granular approach to tsunami runup and inundation. Commun Comput Phys 3:222–249

Watts P, Grilli ST, Kirby JT, Fryer GJ, Tappin DR (2003) Landslide tsunami case studies using a Boussinesq model and a fully nonlinear tsunami generation model. Nat Hazard 3:391–402

Watts P, Grilli ST, Tappin DR, Fryer GJ (2005) Tsunami generation by submarine mass failure. II: predictive equations and case studies. J Waterw Port Coast Ocean Eng 131:298–310

Wils K, Van Daele M, Lastras G, Kissel C, Lamy F, Siani G (2018) Holocene event record of Aysén Fjord (Chilean Patagonia): an interplay of volcanic eruptions and crustal and megathrust earthquakes. J Geophys Res Solid Earth 123:324–343. https://doi.org/10.1002/2017JB014573

Wilson KM, Allen SC, Power HE (2018) The tsunami threat to Sydney Harbour, Australia: modelling potential and historic events. Sci Rep 8:1–18

Zangrando AF, Bjerck HB, Piana EL, Breivik HM, Tivoli AM, Negre J, (2018) Spatial patterning and occupation dynamics during the Early Holocene in an archaeological site from the south coast of Tierra del Fuego: Binushmuka I. Estudios Atacameños (En línea) 31–49